1 # Globally gridded satellite (GridSat) observations for climate
2 # studies

3 Kenneth R. Knapp[1], Steve Ansari[1], Caroline L. Bain[2], Mark A. Bourassa[3], Michael J.
4 Dickinson[4], Chris Funk[5], Chip N. Helms[6], Christopher C. Hennon[7], Christopher D. Holmes[8],
5 George J. Huffman[9], James P. Kossin[1], Hai-Tien Lee[10], Alexander Loew[11], Gudrun
6 Magnusdottir[12]

[1] NOAA National Climatic Data Center, Asheville, North Carolina

[2] University of California at Irvine, Irvine, California now at Met Office, Exeter, Devon, UK

[3] Florida State University, Tallahassee, Florida

[4] Department of Earth and Atmospheric Sciences, The University at Albany/SUNY, Albany,
New York, now at WeatherPredict Consulting, Wakefield, Rhode Island

[5] USGS Center for Earth Resource Observations and Science, Santa Barbara, California

[6] University of North Carolina Asheville, Asheville, North Carolina, now at Florida State
University, Tallahassee, Florida

[7] University of North Carolina Asheville, Asheville, North Carolina

[8] Department of Earth and Planetary Science, Harvard University, Cambridge, Massachusetts

[9] Science Systems and Applications, Inc. and NASA Goddard Space Flight Center, Greenbelt,
Maryland

[10] Cooperative Institute for Climate Studies (CICS), University of Maryland, College Park,
Maryland

[11] Max-Planck-Institute for Meteorology, KlimaCampus, Hamburg, Germany

[12] University of California at Irvine, Irvine, California

8 Capsule Summary: "Calibrated and mapped geostationary data provides historical satellite
9   data to non-satellite experts for studies of weather and climate."

10 Corresponding Author:

11 Kenneth R. Knapp
12 NOAA/National Climatic Data Center
13 151 Patton Ave.
14 Asheville, NC 28801
15 Ken.Knapp@noaa.gov
16 Phone: 828-271-4339
17 Fax: 828-271-4328

18

Abstract

19

20   Geostationary satellites have provided routine, high temporal resolution Earth observations

21   since the 1970s. Despite the long period of record, use of these data in climate studies has been

22   limited for numerous reasons, among them: there is no central archive of geostationary data for

23   all international satellites, full temporal and spatial resolution data are voluminous, and diverse

24   calibration and navigation formats encumber the uniform processing needed for multi-satellite

25   climate studies. The International Satellite Cloud Climatology Project set the stage for

26   overcoming these issues by archiving a subset of the full resolution geostationary data at ~10 km

27   resolution at 3 hourly intervals since 1983. Recent efforts at NOAA's National Climatic Data

28   Center to provide convenient access to these data include remapping the data to a standard map

29   projection, recalibrating the data to optimize temporal homogeneity, extending the record of

30   observations back to 1980, and reformatting the data for broad public distribution. The Gridded

31   Satellite (GridSat) dataset includes observations from the visible, infrared window, and infrared

32   water vapor channels. Data are stored in the netCDF format using standards that permit a wide

33   variety of tools and libraries to quickly and easily process the data. A novel data layering

34   approach, together with appropriate satellite and file metadata, allows users to access GridSat

35   data at varying levels of complexity based on their needs. The result is a climate data record

36   already in use by the meteorological community. Examples include reanalysis of tropical

37   cyclones, studies of global precipitation, and detection and tracking of the intertropical

38   convergence zone.

39

40   With the recent passing of the 50th anniversary of the first U.S. weather satellite,

41   questions on how to best use historical satellite data come to the forefront of the discussion on

42   climate observation. There are now over 30 years of globally sampled geostationary and polar

43   satellite data, and while the visible and infrared imaging instruments on the satellites were not

44   specifically designed for climate purposes, the record has great potential to be used for

45   observational climate studies. With this in mind, NOAA recently embarked on an effort to derive

46   Climate Data Records (CDRs) from environmental satellite data (National Research Council

47   2004), including geostationary satellites. At present, most CDRs derived from historical satellites

48   are based on polar orbiting instruments, such as sea surface temperature data (Reynolds et al.

49   2002). Climatic use of geostationary data has been limited largely to satellite experts – e.g., the

50   international community activities of the Global Energy and Water Experiment (GEWEX) such

51   as the International Satellite Cloud Climatology Project (ISCCP) and the Global Precipitation

52   Climatology Project (GPCP).

53   Numerous issues hinder use of the complete global geostationary data record by the

54   climate research community. First, each country archives its own geostationary data. Thus, to

55   obtain global data, one would access data from the U.S. (for the Geostationary Operational

56   Environmental Satellites, GOES), Europe (for the Meteorological Satellites, Meteosat) and Japan

57   (for the Geostationary Meteorological Satellites, GMS, and Meteorological Satellite, MTSAT).

58   Second, the volume of full resolution data can be unwieldy for any study at climate time-scales.

59   Third, the data format from each agency will be heterogeneous; furthermore, the data from any

60   one agency will likely have multiple file formats. Assuming a user can overcome these hurdles,

61   they must also calibrate (i.e., calculate radiances and brightness temperatures from the data) and

62 navigate (i.e., determine the latitude and longitude for each image pixel) the data from each of

63 the satellites.

64 As mentioned, the ISCCP and GPCP projects are two of the few climate uses of

65 geostationary data prior to 2000. This is due in part to the international collaboration that

66 overcame the hindrances described above. In particular, the ISCCP stored a subset of satellite

67 data at NCDC called ISCCP B1 that included data from each international meteorological

68 satellite. However, necessary information about the data such as file format, navigation

69 algorithms, etc. were not archived. This caused the ISCCP B1 archive to be mostly unusable

70 until a rescue effort rectified these issues (Knapp et al. 2007) and provided access to the data for

71 1983 to present. In addition, further efforts (Knapp 2008a) have expanded the period of record

72 back to 1980.

73 The ISCCP B1 data have since been processed into Gridded Satellite (GridSat) data, a

74 format that is easily accessed and processed by the climate research community at large. This

75 paper describes the construction of the dataset – describing some of the aspects of how the data

76 are provided to facilitate user access – and highlights some of the applications of GridSat. Along

77 the way, the reader is not only encouraged to consider GridSat as a tool for better understanding

78 the Earth's climate, but also as an example of how other observational data could be provided to

79 a broad user community.

GridSat overview

81 GridSat data are derived from the ISCCP B1 data, which are detailed by Knapp (2008a).

82 In short, the data are similar to the Hurricane Satellite (HURSAT) data (Knapp and Kossin

83 2007), but at a global scale. As a result, GridSat's spatial, temporal, and spectral features that are

84   described below are similar to HURSAT. The characteristics of the GridSat data are provided in

85   Table 1.

86   The NOAA Climate Prediction Center (CPC) produces a globally-merged IR product

87   called the CPC-4km product (Janowiak et al. 2001). This product is created in real time and used

88   to monitor global precipitation. Because of the similarity between GridSat and CPC-4km, the

89   details of CPC-4km are provided alongside GridSat in Table 1. The primary difference between

90   the two datasets is that the CPC-4km product is geared toward real-time weather application

91   while GridSat targets long term global processing. For instance, both datasets attempt to reduce

92   inter-satellite differences by intersatellite normalization, however, GridSat also performs

93   temporal normalization via calibration against HIRS during the GridSat period of record. Thus,

94   the data are complementary.

95   GridSat data are provided in an equal angle map projection (also called equirectangular

96   or plate carrée), which facilitates the mapping and subsetting of the data. Since the ISCCP B1

97   native resolution is approximately 8km, the resolution of the equal area grid is 0.07° latitude

98   (~8km at the Equator). The data span the globe in longitude and range from 70°S to 70°N. The

99   spatial and temporal coverage of the satellites contributing to ISCCP B1 is provided in Figure 1 –

100   the so-called "geostationary quilt". While the first year of GridSat data (1980) is mostly

101   composed of satellites in the GOES-East and West positions (Figure 1b), a four-satellite

102   constellation is representative of the period from 1982 through 1998. (e.g., Figure 1b). Failures

103   of satellites often caused a three-satellite configuration but nearly global coverage is still possible

104   (Figure 1d), though at large view zenith angles. Finally, the Indian Ocean gap was filled in 1998,

105   completing the global coverage (Figure 1e). In recent years, coverage has increased with the

106   provision of the Chinese Fen Yung (FY) geostationary satellites and the loan of GOES satellites

5

107   for a South American coverage at 60° west. The satellite intercalibration by Knapp (2008b)

108   effectively stitches each quilt piece together, allowing for a consistent global dataset.

109   **GridSat Channels**

110   In spite of the diversity of satellites and nations providing data, the ISCCP B1 can

111   provide a uniform set of observations for the infrared window (IR) and visible channels – at 11

112   and 0.6 μm, respectively – during the period of record of ISCCP B1 data. Since 1998, the

113   infrared water vapor channel (WVP) near 6.7 microns is also available on a global basis.

114   The IR channel is a window channel (i.e., a region with little atmospheric absorption) that

115   senses the Earth's surface under clear sky conditions, cloud top temperatures of thick clouds, and

116   a combination of cloud and surface for optically thin clouds. Many applications of this channel

117   are discussed below.

118   The visible channel is also a window channel that provides information on clouds and the

119   surface. This channel also has the potential to provide information on Earth radiation budget

120   variables such as aerosols (Knapp 2002) and surface albedo (Loew and Govaerts 2010).

121   The WVP channels are generally centered near 6.7 μm, which is in a water vapor

122   absorption band making it sensitive to humidity in the upper troposphere. This can provide

123   information on circulation patterns. However, this channel has limited global coverage,

124   beginning only in 1998.

125   **Inter-satellite calibration**

126   The data in GridSat use the intercalibration provided by ISCCP calibration efforts

127   (Desormeaux et al. 1993) for the IR and visible channels. The IR channel has also undergone a

128   second intercalibration using the High resolution Infrared Radiation Sounder (HIRS) as a

129   reference, which detected and corrected bias in the ISCCP calibration at cold temperatures after

130   2001 (Knapp 2008b). The WVP channel calibration can be tied to a HIRS upper level water

131   vapor channel (channel 12) but is complicated by the switch in central wavelength between

132   HIRS/2 to HIRS/3 (from 6.7 to 6.5 μm) and is still being tested.

133   Data are calibrated and stored in files as brightness temperature for longwave channels

134   (IR & WVP) and reflectance for the visible channel. The IR data are calibrated following Knapp

135   (2008b), view zenith corrected following Joyce et al. (2001) and parallax-corrected following

136   Janowiak et al. (2001).

137   **GridSat Production**

138   For each 3-hour time slot, the IR, WVP and visible channels on each satellite are mapped

139   to an equal-angle grid using nearest-neighbor sampling. Areas of satellite overlap are retained by

140   storing data in layers (see Figure 2) using the following technique. For each channel, the primary

141   layer retains observations with the nadir-most (i.e., the lowest) view zenith angle, while a

142   secondary layer holds the regions dropped from the first layer. Similarly, a tertiary layer is

143   retained for the third-best view zenith angles (that are dropped from the secondary layer). The

144   extra layers are provided for future intercomparisons and intercalibrations (i.e., developing

145   algorithms for various zenith angles). Furthermore, a satellite can be reconstructed by combining

146   its contributions to each layer (e.g., by taking all the orange portions from each row of Figure 2,

147   one can reconstruct the GOES-11 satellite).

148   In addition to the channel data, satellite identification is stored per pixel with

149   corresponding satellite information: satellite latitude, longitude and radius. So while pixel-level

150   satellite view zenith and azimuth angles are not stored, they can be calculated using the Earth

151 location and the stored satellite position (Soler and Eisemann 1994). Furthermore, calibration

152 information for each channel is provided such that original ISCCP B1 satellite counts can be

153 backed out

154   Data are stored using netCDF (Rew and Davis 1990) and CF conventions that facilitate

155 usage with other software (see sidebar). Channel primary layers (nadir-most observation) are

156 written as 2-dimensional (2D) grids in the netCDF file, which facilitates processing of multiple

157 files (e.g., aggregation of multiple times, etc.). Subsequent layers are written as either 2D grids

158 or staggered arrays, which are 1-dimensional arrays that only record data when they exist.

159 Staggered arrays are more efficient when storing maps where data are mostly missing, as is often

160 the case for the tertiary layer.

Sidebar: netCDF and CF compliance: Simplifying data access and processing

161
162

163   Recent advances in data services allow access and dissemination of data to a broad user

164 community such that data servicing is now more than just putting files on an FTP server. Data

165 servers provide numerous capabilities to users, for example allowing them to download only the

166 data of interest, which saves download bandwidth and research time. Some of the capabilities are

167 summarized below along with a real example of how data processing can be simplified with

168 available tools.

169   The netCDF data format is supported by Unidata and has libraries that allow access to the

170 data from dozens of programming languages. The recent version update of netCDF also allows

171 for data compression that results in smaller storage and bandwidth requirements. The GridSat

172 data are stored in netCDF using the Climate and Forecasting (CF) convention. By complying

173 with CF, GridSat data are stored in a manner that other tools recognize, for example, providing

174   the coordinates of the data variables. In addition, tools such as the netCDF library and netCDF

175   operators (NCO) (Zender 2008) are capable of reading files across the Internet without

176   previously downloading the data.

177   GridSat data are served using the THREDDS data server (TDS) developed by Unidata,

178   which allows users various options for downloading data. The TDS OPeNDAP access allows an

179   OPeNDAP client (such as the NetCDF library, NCO, IDV and more) to remotely subset and

180   download only the desired data slice or pixel. This provides efficient access to very large files or

181   aggregations (i.e., virtual groups of files) without the user needing to download the entire file.

182   The TDS Web Map Service access allows applications such as GIS, Google Earth, or online

183   mapping to directly request rendered images (gif, png, jpeg) from the data server. These images

184   already have a color table applied and can be produced in a variety of predefined projections.

185   The TDS NetCDF Subset Service provides a web-based 'slice-and-dice' service for users. Users

186   may extract a spatial and temporal subset of the data and save the results as CF-compliant

187   NetCDF, XML or comma-separated variable (CSV) text files. Therefore, a variety of user

188   access methods exist that provide interoperability with many existing software tools. Each

189   method can be invoked by a single URL, enabling easy automation and scripting.

190   Numerous tools have been created to simplify the processing of CF compliant data. More

191   than just data visualization, tools like NCO provide command line capabilities to perform

192   averages, concatenations, and more. For instance, sample code is provided in Figure SB1 that

193   processes one month of GridSat IR data, creating diurnally averaged IR brightness temperatures

194   over the Sahara Desert for July 2002. Similar code was used to process the global diurnal trend

195   maps in the outgoing longwave radiation section. The calls to NCO (*ncra* and *ncrcat*) provide a

196   simple means to average IR brightness temperatures (via the –*v* flag) for a specific region (via

197   the *–d* flag) and concatenate the files together. The alternative would be writing hundreds of lines

198   of source code (e.g., C or FORTRAN) to read in the data, calculate the diurnal average, define

199   the output file and write the data. Instead, the seven line shell script accomplishes the same task.

200   The resulting data can then be displayed easily with GrADS (using only 4 commands), for

201   example, to show the mean temperature change from 3 to 15 UTC over the Sahara Desert

202   (Figure SB2).

203   In summary, it is clear that processing gridded netCDF data – such as GridSat – is

204   simplified by CF compliance and the many tools available for serving and processing CF-

205   compliant netCDF data.

Dataset applications for infrared window data

207   Here we present a selection of real-world climatological studies that depend upon

208   GridSat. The aim is to demonstrate the diverse nature of satellite data usage, and emphasize why

209   historic satellite data is of importance to numerous scientific communities. Many of these users

210   are non-expert satellite users who would be otherwise unable to process uncalibrated and

211   unmapped satellite data in a timely manner. The applications of GridSat described below are

212   limited to the IR channel data, which has received the more extensive inter-satellite calibration.

213   The IR data have been applied to tropical cyclones, the Intertropical Convergence Zone (ITCZ),

214   global and regional precipitation monitoring and outgoing longwave radiation.

Tropical cyclones

216   Given the current questions regarding tropical cyclone variability in a warming climate

217   and the challenges posed by the large uncertainties and heterogeneities in the historical tropical

218   records, one very natural application of GridSat is toward the homogenization of these records.

219 GridSat has been used to detect tropical cyclones, estimate their intensity and wind structure, and

220 follow them through their lifetimes from genesis to their demise or transition to extra-tropical

221 storms.

222 *Tropical disturbances and cyclogenesis*

223   Tropical disturbances are early precursors to tropical cyclones. Traditionally,

224 disturbances have been tracked and evaluated according to the Dvorak technique (Dvorak 1975,

225 1984), which estimates intensity based on the shape and evolution of cloud cover. This

226 technique works best for systems nearing tropical cyclone stage; it is much less effective for

227 weaker systems. The GridSat data set is useful for a newer approach that also utilizes surface

228 vector wind information. Scatterometer wind vectors can be used to estimate areal averaged

229 surface vorticity (Bourassa and McBeth-Ford 2010; Sharp et al. 2002). The surface conditions

230 used to identify tropical disturbances are a threshold area-average vorticity of 5.0×10^{-5} s^{-1},

231 combined with a minimum wind speed of 6.3 m s^{-1} within the averaging area. Furthermore, the

232 first two conditions must be met often enough in a 50 km radius area (Bourassa and McBeth-

233 Ford 2010; Gierach et al. 2007). Coverage from a single scatterometer is insufficient to

234 confidently track tropical disturbances. Therefore, Gierach et al. (2007) combined cloud-top IR

235 observations with the surface vorticity to identify likely tropical disturbances. The cloud cover

236 could be tracked to provide continuity between scatterometer observations. This technique

237 proved to be quite effective for the North Atlantic basin (Gierach et al. 2007) and is now being

238 investigated for other hurricane basins.

239   Given the limited period of record of scatterometer data, another approach has been

240 developed that uses only the IR data to detect potential tropical disturbances. One requirement

11

241 for tropical cyclogenesis is the existence of a large area of intense and persistent thunderstorms,

242 called a cloud cluster. During a typical hurricane season in the Atlantic, there are usually more

243 than 100 cloud clusters that form and move across the basin. Cloud clusters are associated with

244 easterly waves, stalled mid-latitude fronts, and large areas of atmospheric instability. Lee (1989)

245 defined a cloud cluster as: being independent of other systems, having a diameter of at least 4°

246 latitude (not elongated) and persisting for at least 24 hours. Owing to their critical importance in

247 the tropical cyclogenesis process, several recent studies (e.g., Hennon and Hobgood 2003) have

248 manually compiled a large dataset of cloud clusters for study, a time-consuming task that

249 involves examining hundreds or thousands of basin-wide IR imagery individually.

250   In contrast, Hennon et al. (2011) objectively identified cloud clusters in GridSat data by

251 testing the IR brightness temperature (Tb) data. The process uses a threshold to detect deep

252 convection, and then applies spatial and temporal analysis to determine whether a region meets

253 the definition of a cloud cluster. Figure 3 shows the frequency (number of clusters per year) of

254 objectively identified cloud cluster tracks for first decade of global coverage (1998-2007). The

255 highest densities are found in the Intertropical and South Pacific convergence zones, North

256 Indian Ocean, and off the west coast of Africa. These areas are consistent with observed areas of

257 cloud cluster activity and tropical cyclogenesis. This cloud cluster dataset spans nearly 30 years

258 and could be applied to several areas of research, including: intraseasonal and interannual

259 studies, impacts of a warming world on cloud cluster activity, and case studies for use in tropical

260 cyclogenesis research (e.g., using Knapp et al. 2010).

261 *Understanding cyclone intensity and structure*

262   Tropical cyclones are monitored and forecasted by a number of forecast agencies

263 worldwide. Most forecast agencies provide estimates of the location and intensity of tropical

264 cyclones in their areas of responsibility, but processes and data have improved over time. This

265 makes the historical record of TC intensity heterogeneous by construction. Conversely, studies of

266 the changes to tropical cyclone intensity require data with no temporal heterogeneities. HURSAT

267 data, in essence, derive from GridSat collocated with tropical cyclones in the IBTrACS data

268 record (Knapp and Kossin 2007), see Figure 4. Kossin et al. (2007a) used HURSAT to

269 objectively estimate TC intensity by exploiting well-known relationships between intensity and

270 the satellite presentation of the storms. Additionally, the wind structure inside the tropical

271 cyclone can be derived from HURSAT (Kossin et al. 2007b), providing information about the

272 extent from the storm center that storm force winds reach. So in addition to the climatic

273 perspective, GridSat data (via HURSAT) also provide an understanding of tropical cyclone

274 conditions throughout their lifetime.

275 *Tropical cyclone transition to extratropical systems*

276   Tropical cyclones moving out of the tropics poleward to the middle latitudes can undergo

277 significant structural and intensity modifications due to changes in the surrounding large-scale

278 environment. In general, these tropical systems are weakening as they accelerate poleward over

279 colder sea surface temperatures (or move over land) and into an increasingly baroclinic

280 environment. Broadly speaking, extratropical transition (ET) is the conversion of a symmetric,

281 vertically stacked, warm core tropical cyclone with maximum intensity in the lower troposphere

282 into an asymmetric, cold core and tilted extratropical cyclone with maximum intensity in the

13

283   upper troposphere. The evolution of the ET is sensitive to the interaction of the decaying tropical

284   cyclone with the mid-latitude circulation; see Jones et al. (2003) for a thorough review. During

285   ET, the cloud and precipitation shield expands ahead and to the left of the tropical cyclone

286   center, in response to the synoptic forcing associated with the approaching mid-latitude trough.

287   ET events can be tremendous rain makers as the large area of synoptically driven ascent can act

288   on abundant tropical moisture. Numerous studies show that ET is common in the Atlantic (Hart

289   and Evans 2001), western Pacific (Klein et al. 2000), and Australian (Foley and Hanstrum 1994;

290   Sinclair 2002) basins, but not the eastern Pacific basin.

291   GridSat, via the HURSAT dataset, is being used to document in detail the remarkable

292   events of late August 1992. During this period, the first ever documented ET in the Eastern

293   Pacific Ocean: Hurricane Lester over the southwestern United States. At the same time,

294   Hurricane Andrew devastated south Florida and made a second landfall along the central

295   Louisiana coast. Andrew was then steered poleward ahead of the same baroclinic system

296   responsible for the ET of Hurricane Lester just days prior. Finally, the upscale impact of Lester

297   and Andrew on the synoptic-scale flow led to the downstream development and the generation of

298   a "vorticity seed" in the western Atlantic. Despite favorable sea-surface temperatures and low

299   vertical wind shear, no tropical system developed. All of which are directly related to each other.

300   **ITCZ Detection**

301   GridSat's coverage in the tropics is ideal for the study of larger scale weather features

302   that may exceed the vision of a single geostationary satellite. The ITCZ is one such feature. It

303   occurs as a narrow band spanning the tropics where the trade winds meet, and is visible as a

304   region of increased convective activity. This highly dynamic and variable weather feature has

305 been studied in observations mostly in a time-averaged sense. The transient nature of the ITCZ

306 makes accurate detection for process studies challenging. Previous studies have used analysis

307 products (e.g., Magnusdottir and Wang 2008), have manually labeled satellite frames and

308 therefore only use a few years of data (e.g., Wang and Magnusdottir 2006), or have thresholded

309 brightness temperature to identify the ITCZ (Waliser and Gautier 1993). The latter has the

310 disadvantage of including convection not associated with the ITCZ. Bain et. al. (2011b)

311 developed a statistical model for ITCZ detection (along with uncertainty measures) and applied it

312 to GridSat for its entire period of record, providing a long record of ITCZ variability in the east

313 Pacific.

314 The statistical model of ITCZ detection objectively identifies the envelope of convection

315 in a probabilistic framework that is described in detail by Bain et. al. (2011b). The method

316 requires that the satellite dataset be reliably calibrated over long periods and available at high

317 temporal resolution, although the model can easily accommodate occasional data gaps. It is also

318 important that there are no noticeable discontinuities when satellites are changed. The GridSat

319 dataset is ideal for this approach. Figure 5 demonstrates the objectively tracked ITCZ in the east

320 Pacific. The black line represents the envelope of convection that the statistical model has

321 determined is part of the ITCZ. Note that some isolated convection is not included as part of the

322 ITCZ since it is determined not to be related to the larger scale feature.

323 Using this technique, a database was created identifying the ITCZ in the east Pacific (90 -

324 180W, 0 - 30N) every 3 hours from 1980 to 2008. The database has been used to construct

325 detailed analysis of the climatology of the ITCZ as well as seasonal and inter-annual variability

326 (Bain et al. 2011b). The additional advantage of the high temporal sampling has also allowed in-

327 depth studies into the diurnal cycle of the ITCZ in Bain et. al. (2011a), where the size of the

15

328 ITCZ as well as the character of clouds within in it were found to vary according to time of day.

329 The ability to use the same dataset for both short timescales and long timescales lends strength to

330 investigations of the ITCZ and is therefore particularly useful for relating climatological and

331 dynamical aspects of the feature.

332 **Precipitation**

333   The detection of precipitation is not wholly unrelated to the above applications, as both

334 tropical cyclones and the ITCZ can cause copious amounts of precipitation. The following details

335 the study of precipitation using GridSat in global and regional studies.

336 *Global precipitation climatologies*

337   Compared to microwave and infrared sensors, which are typically used for the generation

338 of long-term precipitation climatologies (e.g., Adler et al. 2003; Xie and Arkin 1997), GridSat

339 provides complementary information at high temporal and spatial resolution in three different

340 channels. The high spatial resolution of GridSat can help to better identify cloud systems capable

341 of producing rain while the high temporal resolution allows for tracking the development and

342 movement of medium- and large-scale cloud systems. The data from the IR channel can be used

343 to better identify convective cells and therefore resolve precipitating systems with a scale smaller

344 than the footprint of a microwave sensor [similar to the approach of Joyce et al. (2004)]. Merging

345 the multi-spectral and high resolution GridSat data with data from sensors on polar orbiting

346 satellites might be a fruitful pursuit, which could allow for temporal interpolation between

347 subsequent overpasses of a microwave sensor that only provide a few observations per day at a

348 global scale.

349   Erroneous discrimination of optically thin and thick clouds can have a significant effect

350   on uncertainties in precipitation retrieval (Ba and Gruber 2001). Non-precipitating cirrus clouds

351   mistakenly interpreted as thick precipitating clouds contribute to overestimation of rain rate.

352   Differencing between GridSat IR and WVP data allows one to discriminate between optically

353   thin clouds and thick clouds possibly overlaid by cold ice clouds (Turk and Miller 2005). While

354   the WVP channel is primarily sensitive to the water vapor in the upper troposphere, the IR

355   channel is sensitive to the cloud top temperatures. Optically thick clouds reaching the upper

356   troposphere would produce low values in both channels, so the difference between them would

357   be very small. In the opposite case, when optically thin ice clouds overlay ground surface or

358   lower clouds with relatively warm tops, brightness temperature in the IR would be significantly

359   less than the WVP. The same technique could be applied to discriminate cold cloud tops from

360   ground surface covered by snow or ice. Thus, GridSat data will likely have a significant impact

361   on global precipitation climatologies.

362   *Mercury wet deposition: Polluted rain*

363   At regional scales, Holmes (2008, 2010) applied GridSat data to the study of societal

364   impacts of precipitation in the eastern United States. Wet deposition is a major source of mercury

365   to ecosystems, which can then be converted to methylmercury that may bioaccumulate to

366   harmful levels in fish, birds and humans (Lindberg et al. 2007; Mergler et al. 2007;

367   Scheuhammer et al. 2007). Many US water bodies exceed the mercury concentrations allowed

368   by the Clean Water Act, motivating efforts to understand and reduce mercury exposure through

369   precipitation.

370   Mercury deposition in the southeast US is nearly double that in the northeast despite

371 lower anthropogenic emissions in the region, seen in Figure 6a (Environmental Protection

372 Agency 2008; Mercury Deposition Network 2006). Peak seasonal deposition occurs in summer

373 when convective storms are common. This led Guentzel et al. (2001) and Selin and Jacob (2008)

374 to hypothesize a causal link between high-altitude wet scavenging in deep convection and the

375 elevated deposition. Holmes (2008, 2010) tested this hypothesis by correlating IR cloud

376 temperatures from GridSat with mercury deposition measured by the EPA Mercury Deposition

377 Network (MDN). Figure 6a shows data from 8 MDN sites in the southeast during June-

378 September of 2001-2006. Precipitation samples accumulate over 1 week and the associated cloud

379 temperatures are calculated as the average over the collection period of daily minimum

380 temperatures observed within 20 km of the collection site. Deposition clearly increases with

381 colder temperatures (Figure 6b), but this is partially due to large precipitation depths associated

382 with tall, cold clouds. Figure 6c shows that even for equivalent rainfall depths, mercury

383 deposition is about 2 times greater in the samples with the coldest average clouds ($T_b < 240$ K)

384 compared with the warmest ones ($T_b > 260$ K). Ongoing work addresses the dynamical

385 implications of these results.

386 **Precipitation and temperature monitoring in data sparse regions**

387   Another societal implication of precipitation is the availability of food production in

388 regions with little irrigation infrastructure. Adverse trends in rainfall and temperature can disrupt

389 agriculture and pastoral livelihoods that are already being impacted by local and global

390 population growth, expanding economies, and increased demand for limited environmental

391 resources. Therefore, the US Agency for International Development Famine Early Warning

18

392   Systems Network (FEWS NET) has supported the creation and analysis of rainfall and

393   temperature climatologies in food insecure regions. This work has identified significant rainfall

394   declines throughout Eastern Africa with the most dramatic declines in Ethiopia and Kenya (Funk

395   and Brown 2009; Funk et al. 2008; Funk et al. 2005). If rainfall declines or temperature increases

396   have exacerbated food insecurity across the Sahel or Eastern Africa, exactly where have these

397   changes occurred? Our response, along with our ability to guide adaptation efforts, has been

398   limited by sparse *in situ* data. FEWS NET has begun working extensively with the GridSat data,

399   which may help us make much finer resolution maps of rainfall and air temperatures over a

400   thirty-year period.

401   We provide here an example based on July-September rainfall and air temperature for

402   eastern Africa and the Sahel. The first analysis step involves the separation of cold and warm IR

403   values for each observation time. For each four-month season, the ~120 3-hourly time-slices are

404   sorted, and the 10th (cold) and 90th (warm) percentiles retained. The 10th and 90th percentile fields

405   are then averaged across the eight 3-hour periods. The result is a field of the mean 10th and 90th

406   percentile values for each July-September, from 1980 to 2008. The exciting thing about these

407   fields is that they effectively capture spatial variations in both temperature and rainfall. The 10th

408   percentile fields correspond with the height of cold clouds, and effectively distinguish areas

409   receiving heavy convective precipitation from those without. Conversely, the 90th percentile

410   fields typically capture near-surface emissions that are related to land temperature.

411   Next, GridSat fields were averaged over two ten-year time periods: 1999-2008 and 1984-

412   1993. These were then correlated with averages of *in situ* temperature and station data for the

413   same periods. (where explained variances exceeded 70% for both parameters). We then use a

414   moving window regression model to build a localized equation translating each IR value into a

415   10 km monthly mean temperature or precipitation. The mean 1999-2008 July-September

416   temperature field is in the top-left of Figure 7. High mountainous areas in Kenya, Ethiopia and

417   near the border of Cameroon and Nigeria are cool, while the sands of the Sahara and the Afar

418   region of Ethiopia are very warm. Interactions between these mountains and the larger scale

419   circulation bring heavy rains to western Ethiopia, and the inter-tropical front stretches across the

420   Sahel (top-right). The region is beset with very strong environmental gradients that shift over

421   time. These variations can be mapped by looking at decadal differences (here the difference

422   between the 1984-1993 and 1999-2008 averages). Such differences may relate to climate change

423   or may be simply due to inherent climate variability. In either case, decadal fluctuations can

424   impact food security, hydrological resources, and environmental sustainability. The GridSat data

425   help us capture shifts in these gradients, building a high resolution picture of change.

426   Looking at the temperature changes (Figure 7, bottom left), a substantial warming signal

427   is apparent; temperatures appear to increase everywhere but some regions more than others. This

428   signal also appears in the station data, with simple averages taken across all the in situ

429   observations exhibiting a slope of 0.05 °C per year (r^2=0.44) with other months exhibiting

430   similar trends. Spatially, however, the strongest warming (>1° C since 1984-1993) appears

431   across a coherent area stretching from Western Kenya and Ethiopia across the Zaire basin. July-

432   Setpember rainfall, on the other hand, exhibits increases across northern Ethiopia and most of the

433   Sahel. Decreases are found across eastern Ethiopia, most of Kenya and Uganda, and the Zaire

434   basin.

435   The spatial detail of these maps should help us understand and adapt to decadal climate

436   variations. From a food security perspective, three patterns emerge: i) a dangerous warming

437   trend across all the Sahel and eastern Africa, ii) combined warming and drying over the last ten

438   years across southwestern Ethiopia and southern Sudan, and iii) a smaller reduction in rainfall

439   near the border of Mali and Senegal . While the GridSat-enhanced analyses are still evolving, it

440   seems likely that these data will substantially improve our ability to track rainfall and

441   temperature changes, enhancing our ability to adapt in a changing world.

442   **Outgoing Longwave Radiation**

443   The Earth radiation budget describes the distribution of radiative energy in the Earth-

444   atmosphere system. The observations of Earth radiation budget parameters at the top of the

445   atmosphere have been performed from both operational and experimental satellites since the

446   1970s. The long and continuous time series of Earth radiation budget parameters, e.g., the

447   outgoing longwave radiation (OLR), is valuable for climate change studies and monitoring. The

448   polar orbiters provide fairly uniform spatial and angular sampling from a given instrument, but

449   with relatively poor temporal sampling resolution. Geostationary satellite observations provide

450   information on the diurnal variation that is essential for deriving such time series accurately.

451   The HIRS OLR climate data record was generated with a set of climatological OLR

452   diurnal models (Lee et al. 2007) that help to reduce the monthly OLR errors resulting from the

453   orbital drift of polar-orbiting satellites. Although these models are self-consistent with the HIRS

454   OLR retrievals, for error budgeting purposes, we would like to assess whether these diurnal

455   models were truly representative and how significant the inter-annual variations can be. Figure 8

456   shows the comparison of the HIRS climatological OLR diurnal models for August 2002 with

457   those derived from the GridSat IR data. Some disagreements are apparent for certain

458   regions/climate types Nevertheless, for the majority, they seem to share a high degree of

459   similarity, both in shape and in phase. These results provide us confidence in the quality and

460   guidance for future improvement of the OLR climate data record production. Similar

461   comparisons are necessary for other seasons and years.

462   A hybrid OLR product can then be generated using HIRS observations and GridSat

463   following Leet et al. (2004), similar in design to that used for the Cloud and the Earth Radiant

464   Energy System (CERES; Young et al. 1998). Such a combination would take advantage of both

465   the accuracy of the HIRS OLR retrieval and the precise diurnal variation signal in geostationary

466   observations. This product will improve the temporal integral accuracy for the HIRS climate data

467   record and possibly allow product generation at a temporal resolution finer than monthly, e.g.,

468   daily or pentad, which would benefit some dynamical diagnostic and precipitation estimation

469   applications.

470   ## Future Work

471   **Future applications using visible and water vapor channels**

472   The bulk of the applications so far have focused on the IR channel, however many areas

473   of study exist for the global inter-calibrated visible and WVP channels. The visible channel is

474   sensitive to clouds and in some regions aerosols as well. Aerosols have a significant role in our

475   daily lives by affecting human health and in our understanding of the Earth's radiation budget

476   via the uncertainty in how much solar radiation they reflect to space versus absorb (in addition to

477   how they affect cloud optical properties and lifetime). Knapp (2002) defined a means to detect

478   the aerosol signal in satellite observations. When this technique is applied to visible GridSat data,

479   many ground sites – Aerosol Robotic Network sites (Holben et al. 1998) – show a strong aerosol

480   signal that implies (given a good cloud algorithm) aerosols can be retrieved from GridSat.

481   GridSat data also have the potential to help accurately determine shortwave and

482   longwave radiation fluxes at the regional to global scale. The Earth's surface albedo is a key

483   terrestrial variable in these flux calculations. While surface albedo data are available from the

484   MODIS sensor since 2000 (Schaaf et al. 2002), long term surface albedo data products that cover

485   multiple decades previously could only rely on operational weather satellites that were not

486   designed for climate monitoring. The general potential to derive global maps of surface albedo

487   from mosaics of geostationary observations has been shown by Govaerts et al. (2008) and the

488   GridSat data might be used for the retrieval of global fields of surface albedo in this way.

489   However a recent study (Loew and Govaerts 2010) has shown that uncertainties in the

490   characterization of the spectral response function of the older generation of geostationary

491   satellites might result in systematic biases and trends in multi-decadal surface albedo data

492   products An appropriate assessment of the uncertainties of each sensor's spectral characteristics

493   and their impact on surface albedo estimates is therefore inevitable for the generation of essential

494   climate records of surface albedo and surface radiation budget from GridSat data.

495   The WVP channel provides information on energetics of the upper troposphere. The

496   channel is sensitive to a broad region of upper tropospheric humidity that can provide

497   information on the distribution and transport of water vapor in the troposphere (Soden and

498   Bretherton 1993; Tian et al. 2004). This channel also has the potential to provide information on

499   water vapor entering the stratosphere (Schmetz et al. 1997) via overshooting convective clouds.

500   In such cases, the WVP channel can be warmer than the IR channel for convection that

501   penetrates the tropopause. GridSat data – in providing global coverage for both channels – has

502   the potential to help monitor the transport of water vapor.

503 **Dataset improvements**

504   Given the widespread use of the GridSat dataset, efforts are underway to further improve

505 the dataset. The ISCCP project is revamping software processing to produce higher resolution

506 cloud products based on ISCCP B1 data. As part of this work, the pixel level cloud mask will be

507 incorporated into GridSat, providing information on the presence of clouds in the GridSat data.

508   A new version of the GPCP datasets is now in development, with the GridSat data as one

509 key upgrade. Using GridSat, spatial resolutions of GPCP will likely increase: the monthly GPCP

510 product from 2.5° lat. to 0.5° and the daily will shift from 1° to 0.25°. In addition, the daily

511 dataset eventually could be pushed from its current start of October 1996, perhaps to the start of

512 Special Sensor Microwave Imager data in July 1987. For both datasets, the current latitude

513 bounds for GPCP geostationary IR data of 40°N-40°S will be relaxed to the entire useful range

514 of simple IR-based estimates, around latitude 50°- in the summer hemisphere.

515   Furthermore, the use of GridSat data by non-satellite experts suggests that a similar

516 remapping would benefit other satellite data. For example, instruments on polar orbiting

517 satellites could be remapped in a similar way as GridSat. This would likely make data – like that

518 from AVHRR, HIRS and other instruments – more widely available to a broad base of users.

519   Lastly, the observations that comprise the GridSat data are being revised. The visible and

520 WVP radiances will soon be intercalibrated (the latter is hindered by a change in HIRS water

521 vapor central wavelength). The IR satellite view zenith angle correction should be improved as

522 well. The current algorithm (Joyce et al. 2001) was developed for satellites in use in 2000

523 (GOES-8,10, GMS-5, Meteosat-5,7) however, the corrections are likely satellite dependent

524 (particularly the older satellites that had more water vapor contamination in the infrared window

525   channels). An updated satellite zenith angle correction that is satellite dependent would decrease

526   the remnant seams still apparent in GridSat IR data.

Summary
527

528   Geostationary satellites have now been providing weather data for 50 years. Much of

529   these data have been neglected by climate observation studies due to difficulties with calibration

530   and data processing over such a long period. Collection and data ownership rights were spread

531   out across several international agencies. The ISCCP project is overcoming these barriers and

532   this paper has presented details on the most up-to-date and easily accessible global satellite

533   record: GridSat.

534   This new record provides equal-angle gridded uniform observations of brightness

535   temperatures every 3 hours from 1980 to the present. We have demonstrated the multiple and

536   diverse uses of the data – from predicting drought and food security in Africa to the detailed and

537   historical tracking of hurricanes. This only touches on some of the potential uses of GridSat.

538   Accurate records of global atmospheric fields are essential for future research on climate change

539   as well as the understanding of the planet's meteorology.

540   By reconstructing past satellite data and combining them with current satellite

541   observations, a seamless data record has been obtained for the study of the Earth's atmospheric

542   state. In addition, GridSat has given a wide range of users very easy access to this new data

543   record. Development of GridSat will continue, focusing on improving the current data files and

544   supporting more applications.

Acknowledgements

References

Adler, R. F., and Coauthors, 2003: The Version-2 Global Precipitation Climatology Project
    (GPCP) Monthly Precipitation Analysis (1979-Present). *Journal of Hydrometeorology*, **4,**
    1147-1167.

Ba, M. B., and A. Gruber, 2001: GOES Multispectral Rainfall Algorithm (GMSRA). *Journal of
    Applied Meteorology*, **40,** 1500-1514.

Bain, C. L., G. Magnusdottir, P. Smyth, and H. Stern, 2011a: The diurnal cycle of the ITCZ in
    the east Pacific. *Journal of Geophysical Research*, **In preparation**.

Bain, C. L., J. De Paz, J. Kramer, G. Magnusdottir, P. Smyth, H. Stern, and C.-C. Wang, 2011b:
    Detection of the ITCZ in the east Pacific using Markov random fields on instantaneous
    satellite data. *Journal of Climate*, **Submitted**.

Bourassa, M. A., and K. McBeth-Ford, 2010: Uncertainty in Scatterometer-Derived Vorticity.
    Journal of Atmospheric and Oceanic Technology, **27,** 594-603.

Desormeaux, Y., W. B. Rossow, C. L. Brest, and G. G. Campbell, 1993: Normalization and
    Calibration of Geostationary Satellite Radiances for the International Satellite Cloud
    Climatology Project. *Journal of Atmospheric and Oceanic Technology*, **10,** 304-325.

568 Dvorak, V. F., 1975: Tropical Cyclone Intensity Analysis and Forecasting from Satellite

569   Imagery. *Monthly Weather Review*, **103,** 420-430.

570 ——, 1984: *Tropical cyclone intensity analysis using satellite data.* National Oceanic and

571   Atmospheric Administration, National Environmental Satellite, Data, and Information

572   Service, 47 pp.

573 Environmental Protection Agency, 2008: Model-based analysis and tracking of airborne mercury

574   emissions to assist in watershed planning. *United States Environmental Protection*

575   *Agency*, 350 pp.

576 Foley, G. R., and B. N. Hanstrum, 1994: The Capture of Tropical Cyclones by Cold Fronts off

577   the West Coast of Australia. *Weather and Forecasting*, **9,** 577-592.

578 Funk, C., and M. Brown, 2009: Declining global per capita agricultural production and warming

579   oceans threaten food security. *Food Security*, **1,** 271-289.

580 Funk, C., M. Dettinger, J. C. Michaelsen, J. P. Verdin, M. E. Brown, M. Barlow, and A. Hoell,

581   2008: Warming of the Indian Ocean threatens eastern and southern African food security

582   but could be mitigated by agricultural development. *Proceedings of the National*

583   *Academy*, **105,** 11081-11086.

584 Funk, C., G. Senay, A. Asfaw, J. P. Verdin, G. Eilerts, J. C. Michaelsen, S. Amer, and R.

585   Choularton, 2005: Recent Drought Tendencies in Ethiopia and equatorial-subtropical

586   eastern Africa. *Vulnerability to Food Insecurity: Factor Identification and*

587   *Characterization Rep. 01/2005*, 13 pp.

588 Gierach, M. M., M. A. Bourassa, P. Cunningham, J. J. O'Brien, and P. D. Reasor, 2007:

589   Vorticity-Based Detection of Tropical Cyclogenesis. *Journal of Applied Meteorology and*

590   *Climatology*, **46,** 1214-1229.

591   Govaerts, Y. M., A. Lattanzio, M. Taberner, and B. Pinty, 2008: Generating global surface

592   albedo products from multiple geostationary satellites. *Remote Sensing of Environment*,

593   **112,** 2804-2816.

594   Guentzel, J. L., W. M. Landing, G. A. Gill, and C. D. Pollman, 2001: Processes Influencing

595   Rainfall Deposition of Mercury in Florida. *Environmental Science & Technology*, **35,**

596   863-873.

597   Hart, R. E., and J. L. Evans, 2001: A Climatology of the Extratropical Transition of Atlantic

598   Tropical Cyclones. *Journal of Climate*, **14,** 546-564.

599   Hennon, C. C., and J. S. Hobgood, 2003: Forecasting Tropical Cyclogenesis over the Atlantic

600   Basin Using Large-Scale Data. *Monthly Weather Review*, **131,** 2927-2940.

601   Hennon, C. C., C. N. Helms, K. R. Knapp, and A. R. Bowen, 2011: An Objective Algorithm for

602   Detecting and Tracking Tropical Cloud Clusters: Implications for Tropical Cyclogenesis

603   Prediction. *Journal of Atmospheric and Oceanic Technology*, **Submitted**.

604   Holben, B. N., and Coauthors, 1998: AERONET - A federated instrument network and data

605   archive for aerosol characterization. *Remote Sensing of the Environment*, **66,** 1-16.

606   Holmes, C. D., 2008: Mercury deposition to the Gulf Coast region from deep convection and

607   long-range atmospheric transport. *AGU Fall Meeting*, San Francisco, CA, Eos

608   Transactions.

609   ——, 2010: Thunderstorms increase mercury concentration in rainfall, **In preparation**.

610   Janowiak, J. E., R. J. Joyce, and Y. Yarosh, 2001: A real-time global half-hourly pixel-resolution

611   infrared dataset and its applications. *Bulletin of the American Meteorological Society*, **82,**

612   205-217.

613   Jones, S. C., and Coauthors, 2003: The Extratropical Transition of Tropical Cyclones: Forecast

614   Challenges, Current Understanding, and Future Directions. *Weather and Forecasting*, **18,**

615   1052-1092.

616   Joyce, R., J. Janowiak, and G. Huffman, 2001: Latitudinally and Seasonally Dependent Zenith-

617   Angle Corrections for Geostationary Satellite IR Brightness Temperatures. *Journal of*

618   *Applied Meteorology*, **40,** 689-703.

619   Joyce, R. J., J. E. Janowiak, P. A. Arkin, and P. Xie, 2004: CMORPH: A Method that Produces

620   Global Precipitation Estimates from Passive Microwave and Infrared Data at High

621   Spatial and Temporal Resolution. *Journal of Hydrometeorology*, **5,** 487-503.

622   Klein, P. M., P. A. Harr, and R. L. Elsberry, 2000: Extratropical Transition of Western North

623   Pacific Tropical Cyclones: An Overview and Conceptual Model of the Transformation

624   Stage. *Weather and Forecasting*, **15,** 373-395.

625   Knapp, K. R., 2002: Quantification of aerosol signal in GOES-8 visible imagery over the U.S.

626   *Journal of Geophysical Research*, **107,** 10.1029/2001JD002001.

627   ——, 2008a: Scientific data stewardship of International Satellite Cloud Climatology Project B1

628   global geostationary observations. *Journal of Applied Remote Sensing*, **2,** 023548

629   ——, 2008b: Calibration of long-term geostationary infrared observations using HIRS. *Journal*

630   *of Atmospheric and Oceanic Technology*, **25,** 183-195.

631   Knapp, K. R., and J. P. Kossin, 2007: New global tropical cyclone data from ISCCP B1

632   geostationary satellite observations. *Journal of Applied Remote Sensing*, **1,** 013505

633   Knapp, K. R., J. J. Bates, and B. Barkstrom, 2007: Scientific Data Stewardship: Lessons learned

634   from a satellite data rescue effort. *Bulletin of the American Meteorological Society*, **88,**

635   1359-1361.

636   Knapp, K. R., M. C. Kruk, D. H. Levinson, H. J. Diamond, and C. J. Neumann, 2010: The

637   International Best Track Archive for Climate Stewardship (IBTrACS): Centralizing

638   tropical cyclone best track data. *Bulletin of the American Meteorological Society*, **91,**

639   363-376.

640   Kossin, J. P., K. R. Knapp, D. J. Vimont, R. J. Murnane, and B. A. Harper, 2007a: A globally

641   consistent reanalysis of hurricane variability and trends. *Geophysical Research Letters*,

642   **34,** L04815.

643   Kossin, J. P., J. A. Knaff, H. I. Berger, D. C. Herndon, T. A. Cram, C. S. Velden, R. J. Murnane,

644   and J. D. Hawkins, 2007b: Estimating hurricane wind structure in the absence of aircraft

645   reconnaissance. *Weather and Forecasting*, **22,** 89-101.

646   Lee, C. S., 1989: Observational Analysis of Tropical Cyclogenesis in the Western North Pacific.

647   Part I: Structural Evolution of Cloud Clusters. *Journal of Atmospheric Science*, **46,** 2580-

648   2598.

649   Lee, H.-T., A. K. Heidinger, A. Gruber, and R. G. Ellingson, 2004: The HIRS Outgoing

650   Longwave Radiation product from hybrid polar and geosynchronous satellite

651   observations. *Advances in Space Research*, **33**.

652   Lee, H.-T., A. Gruber, R. G. Ellingson, and I. Laszlo, 2007: Development of the HIRS Outgoing

653   Longwave Radiation climate data set. *Journal of Atmospheric and Oceanic Technology*,

654   **24,** 2029-2047.

655   Lindberg, S., and Coauthors, 2007: A Synthesis of Progress and Uncertainties in Attributing the

656   Sources of Mercury in Deposition. *AMBIO: A Journal of the Human Environment*, **36,**

657   19-33.

658   Loew, A., and Y. Govaerts, 2010: Towards Multidecadal Consistent Meteosat Surface Albedo

659   Time Series. *Remote Sensing*, **2,** 957-967.

660   Magnusdottir, G., and C.-C. Wang, 2008: Intertropical Convergence Zones during the Active

661   Season in Daily Data. *Journal of Atmospheric Science*, **65,** 2425-2436.

662   Mercury Deposition Network, 2006: National Atmospheric Deposition Program 2005 Annual

663   Summary. 16 pp.

664   Mergler, D., H. A. Anderson, L. H. M. Chan, K. R. Mahaffey, M. Murray, M. Sakamoto, and A.

665   H. Stern, 2007: Methylmercury Exposure and Health Effects in Humans: A Worldwide

666   Concern. *AMBIO: A Journal of the Human Environment*, **36,** 3-11.

667   National Research Council, 2004: Climate Data Records from Environmental Satellites, 116 pp.

668   Rew, R., and G. Davis, 1990: NetCDF: an interface for scientific data access. *Computer*

669   *Graphics and Applications, IEEE*, **10,** 76-82.

670   Reynolds, R. W., N. A. Rayner, T. M. Smith, D. C. Stokes, and W. Wang, 2002: An Improved In

671   Situ and Satellite SST Analysis for Climate. *Journal of Climate*, **15,** 1609-1625.

672   Schaaf, C. B., and Coauthors, 2002: First operational BRDF, albedo nadir reflectance products

673   from MODIS. *Remote Sensing of Environment*, **83,** 135-148.

674   Scheuhammer, A. M., M. W. Meyer, M. B. Sandheinrich, and M. W. Murray, 2007: Effects of

675   Environmental Methylmercury on the Health of Wild Birds, Mammals, and Fish.

676   *AMBIO: A Journal of the Human Environment*, **36,** 12-19.

677   Schmetz, J., S. A. Tjemkes, M. Gube, and L. van de Berg, 1997: Monitoring deep convection

678   and convective overshooting with METEOSAT. *Advances in Space Research*, **19,** 433-

679   441.

680 Selin, N. E., and D. J. Jacob, 2008: Seasonal and spatial patterns of mercury wet deposition in

681   the United States: Constraints on the contribution from North American anthropogenic

682   sources. *Atmospheric Environment*, **42,** 5193-5204.

683 Sharp, R. J., M. A. Bourassa, and J. J. O'Brien, 2002: Early Detection of Tropical Cyclones

684   Using Seawinds-Derived Vorticity. *Bulletin of the American Meteorological Society*, **83,**

685   879-889.

686 Sinclair, M. R., 2002: Extratropical Transition of Southwest Pacific Tropical Cyclones. Part I:

687   Climatology and Mean Structure Changes. *Monthly Weather Review*, **130,** 590-609.

688 Soden, B. J., and F. P. Bretherton, 1993: Upper Tropospheric Relative Humidity From the GOES

689   6.7 μm Channel: Method and Climatology for July 1987. *J. Geophys. Res.*, **98,** 16669-

690   16688.

691 Soler, T., and D. W. Eisemann, 1994: Determination of look angles to geostationary

692   communication satellites. *J. Surv. Eng. ACSE*, **120,** 115-127.

693 Tian, B. J., B. J. Soden, and X. Q. Wu, 2004: Diurnal cycle of convection, clouds, and water

694   vapor in the tropical upper troposphere: Satellites versus a general circulation model.

695   *Journal of Geophysical Research-Atmospheres*, **109,** D10101.

696 Turk, F. J., and S. D. Miller, 2005: Toward improved characterization of remotely sensed

697   precipitation regimes with MODIS/AMSR-E blended data techniques. *IEEE*

698   *Transactions on Geoscience and Remote Sensing*, **43,** 1059-1069.

699 Waliser, D. E., and C. Gautier, 1993: A Satellite-derived Climatology of the ITCZ. *Journal of*

700   *Climate*, **6,** 2162-2174.

701 Wang, C.-C., and G. Magnusdottir, 2006: The ITCZ in the Central and Eastern Pacific on

702   Synoptic Time Scales. *Monthly Weather Review*, **134,** 1405-1421.

703   Xie, P., and P. A. Arkin, 1997: Global Precipitation: A 17-Year Monthly Analysis Based on

704   Gauge Observations, Satellite Estimates, and Numerical Model Outputs. *Bulletin of the*

705   *American Meteorological Society*, **78,** 2539-2558.

706   Young, D. F., P. Minnis, D. R. Doelling, G. G. Gibson, and T. Wong, 1998: Temporal

707   Interpolation Methods for the Clouds and the Earth's Radiant Energy System (CERES)

708   Experiment. *Journal of Applied Meteorology*, **37,** 572-590.

709   Zender, C. S., 2008: Analysis of self-describing gridded geoscience data with netCDF Operators

710   (NCO). *Environmental Modelling & Software*, **23,** 1338-1342.

711

712

713

Figure Captions

Figure 1 – a) Time series of ISCCP B1 geostationary observational coverage at the Equator (shading limited to a view zenith angle of 60° for illustrative purposes). b-e) Sample GridSat coverage for typical satellite coverages: b) Two-satellite coverage with only GOES-East and -West in 1980, c) Four-satellite coverage that is typical of most of the period from 1982 through 1998, d) typical three-satellite coverage when the U.S. was operating only one satellite (e.g., 1985-1987 or 1989-1992) and e) five-satellite coverage that is typical of the current era (1998 to present).

Figure 2 - Merged GridSat IR image (left) from 1 Jan. 2008 with satellite identification (right). Top row is the nadir-most observations, followed by the second-most and third-most nadir observations (second and third rows, respectively). The satellites FY-2C, GOES-11, GOES-12, Meteosat-7, Meteosat-9, MTSAT-1R are color-coded as red, orange, yellow, green, blue, and violet.

Figure 3 – Cloud cluster track frequency (clusters per year within 55km of any point) for the first decade of global satellite coverage (1998-2007). Contour levels are set at 1, 5 and 10 per year.

Figure 4 - HURSAT image of 1992 Hurricane Andrew from August 23, 1992 along with a time series of its maximum sustained wind (in knots).

Figure 5 - Example of ITCZ detection in the east Pacific using the statistical model for 18 August 2000 at 2100 UTC. Shading represents IR temperature from GridSat, the black line outlines the identified location of the ITCZ. The North American coastline is outlined in white.

Figure 6 - (A) Mercury wet deposition in the eastern United States for 2005. Stars show sites analyzed here. (B) Mercury wet deposition for summers 2001-2006 and mean infrared (IR) cloud temperature from GridSat IR. See text for IR temperature averaging method. (C) Mercury wet

737 deposition and precipitation for three different cloud temperature ranges. Lines show mean

738 concentration in 50 mm precipitation bins for the coldest (temperature < 240K) and warmest

739 (temperature > 260K) clouds. [Figure adapted from (Holmes 2008, 2010) with deposition map

740 adapted from (Mercury Deposition Network 2006)]

741 Figure 7 – July-September (JJAS) air temperature and rainfall estimates based on combinations

742 of GridSat infrared fields and in situ station observations. The top two panels show decadal

743 average air temperature (left) and rainfall (right) for the 1999-2008 period. The bottom panels

744 show the differences between these decadal averages and the 1984-1993 average (the 1999-2008

745 average minus the 1984-1993 average).

746 Figure 8 - Comparison of diurnal OLR models from the HIRS climatology and GridSat for

747 August 2002. The GridSat OLR helps to verify the representativeness of the climatological OLR

748 diurnal models used in the production of the HIRS OLR climate data record. The arrows in the

749 central panel indicate the phases of the OLR diurnal models with the 12 o'clock local time

750 pointing north, running counter-clockwise. The surrounding plots compare the diurnal models

751 for selected regions with distinctively different types of diurnal variations. The mean values of

752 GridSat OLR in each diurnal plot were adjusted to those of the HIRS to aid visual comparison.

753

754

Tables

756   Table 1 - Summary of similarities and differences between the CPC-4km product and the

757   GridSat dataset.

	CPC-4km	GridSat
Spatial resolution	4km	8km
Temporal resolution	30 min	180 min
Channels	1 (IR)	3 (IR, WVP, visible)
Monthly Volume *(uncompressed)*	45 GB	40 GB
Period of record	2000-present	1980-present
Intersatellite normalization	Yes	Yes
Temporal normalization	No	Yes
Format	Unformatted binary	netCDF

758

759 **Figures**
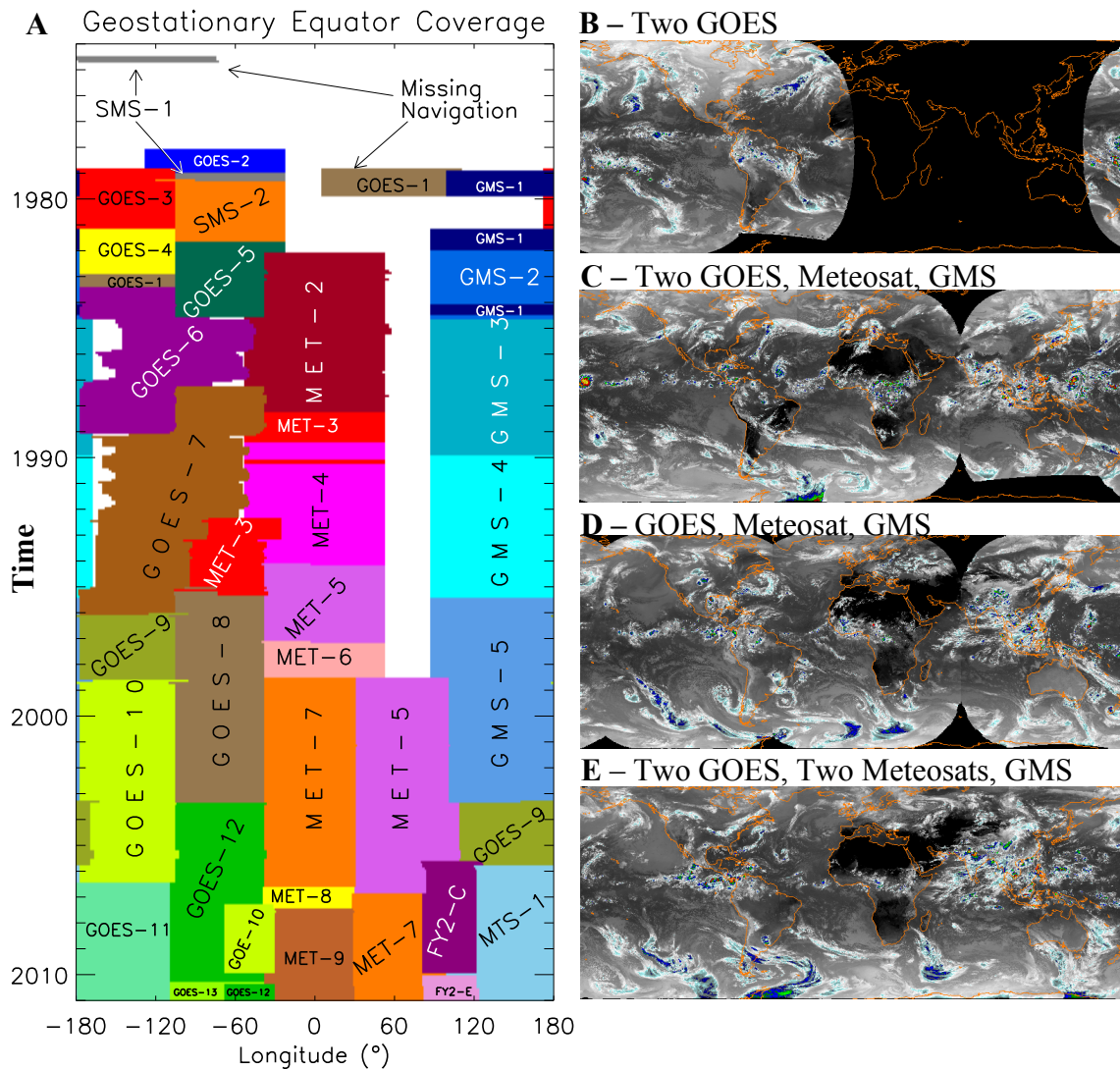
Figure 1 – a) Time series of ISCCP B1 geostationary observational coverage at the Equator (shading limited to a view zenith angle of 60° for illustrative purposes). b-e) Sample GridSat coverage for typical satellite coverages: b) Two-satellite coverage with only GOES-East and -West in 1980, c) Four-satellite coverage that is typical of most of the period from 1982 through 1998, d) typical three-satellite coverage when the U.S. was operating only one satellite (e.g., 1985-1987 or 1989-1992) and e) five-satellite coverage that is typical of the current era (1998 to present).

768
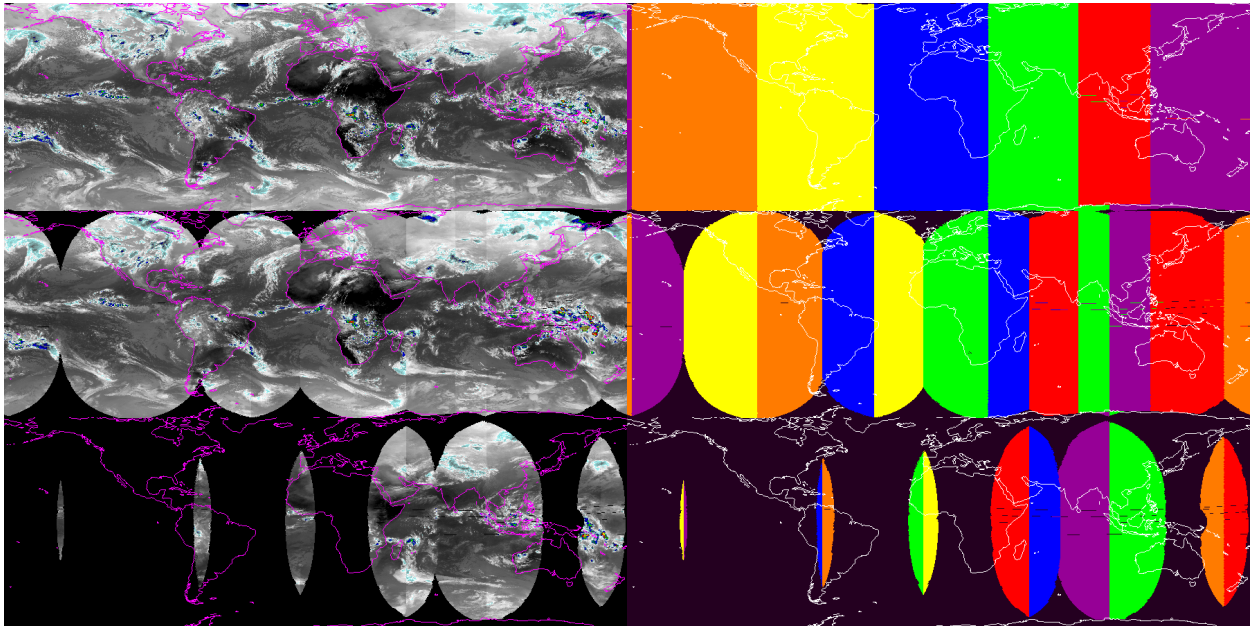
769

770 Figure 2 - Merged GridSat IR image (left) from 1 Jan. 2008 with satellite identification (right).

771 Top row is the nadir-most observations, followed by the second-most and third-most nadir

772 observations (second and third rows, respectively). The satellites FY-2C, GOES-11, GOES-12,

773 Meteosat-7, Meteosat-9, MTSAT-1R are color-coded as red, orange, yellow, green, blue, and

774 violet. Black regions denote missing data.

SWF/GIF

776 Animation location:

777 ftp://eclipse.ncdc.noaa.gov/pub/misc/kknapp/bams_grisat/GriSat-Construction.gif or

778 ftp://eclipse.ncdc.noaa.gov/pub/misc/kknapp/bams_grisat/GridSat-Construction.swf

779

780
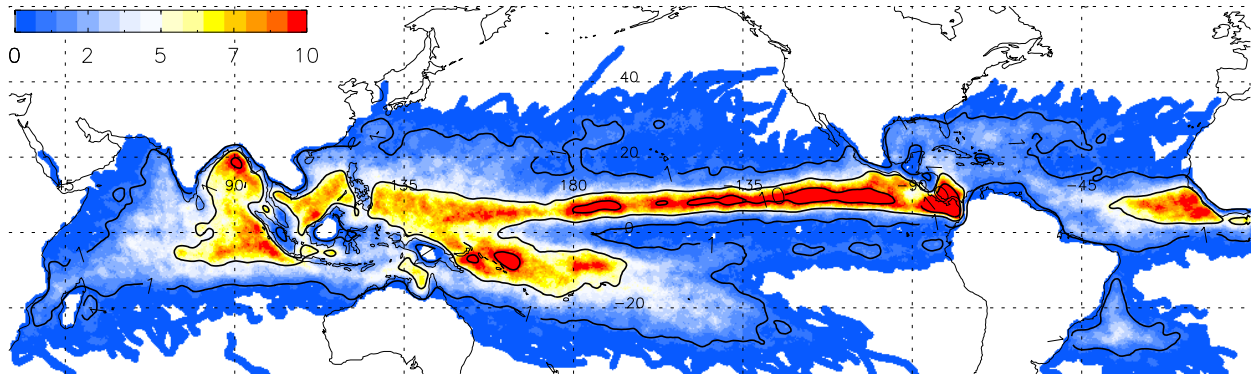
782 Figure 3 – Cloud cluster track frequency (clusters per year within 55km of any point) for the first

783 decade of global satellite coverage (1998-2007). Contour levels are set at 1, 5 and 10 per year.

784 Clusters over land and those that formed north of 30 degrees latitude were filtered out.

785

786

787

788
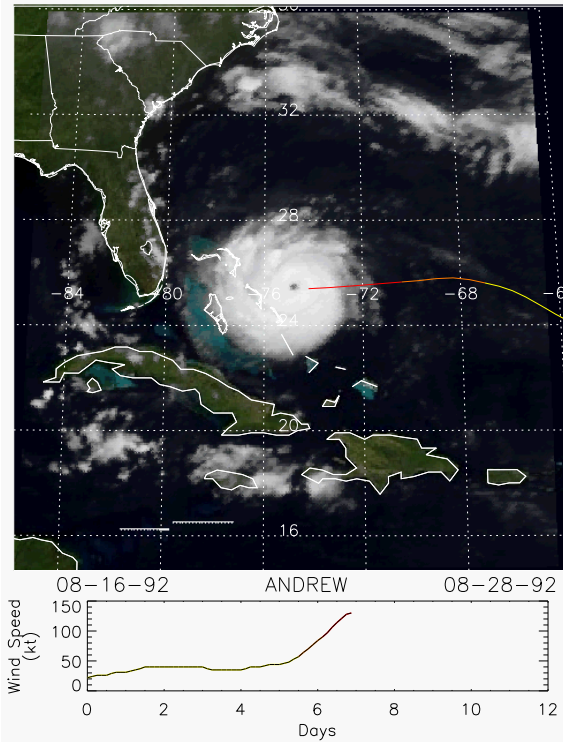
789

790 Figure 4 - HURSAT image of 1992 Hurricane Andrew from August 23, 1992 along with a time

791 series of its maximum sustained wind (in knots).

MPEG/GIF/SWF

793 Animation location

794   ftp://eclipse.ncdc.noaa.gov/pub/hursat/b1/v03/mpg/1992230NA11325-AND.mpg

795 (right click link and "Save as…" then open using Windows Media Player, a codec may be

796 required)

797 ftp://eclipse.ncdc.noaa.gov/pub/misc/kknapp/bams_grisat/andrew.gif or

798 ftp://eclipse.ncdc.noaa.gov/pub/misc/kknapp/bams_grisat/andrew.swf

799

800
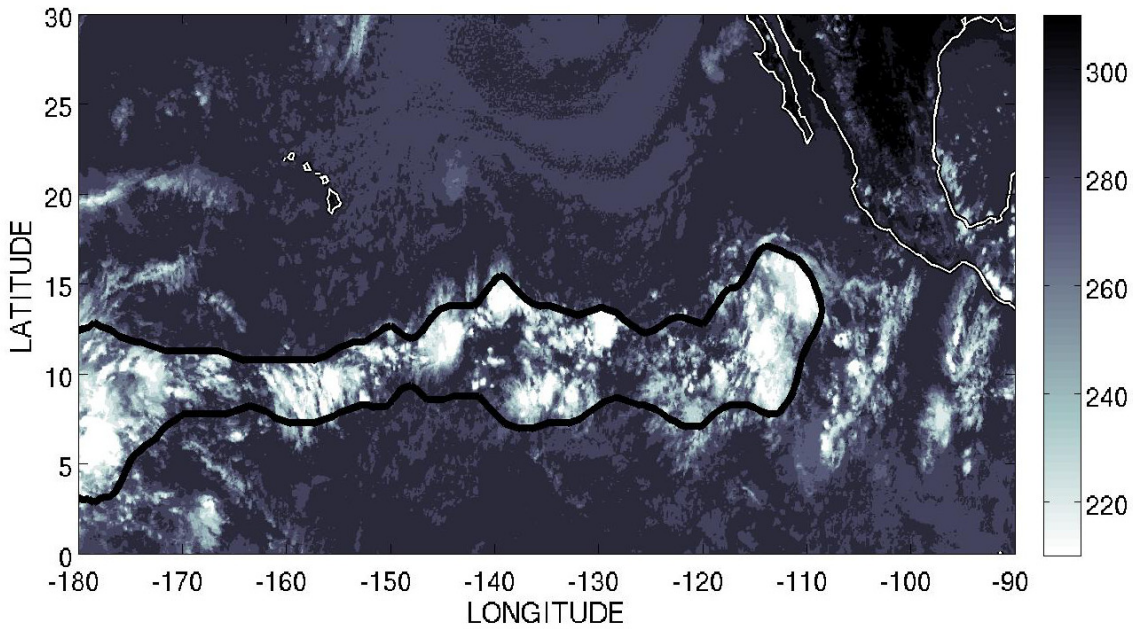
801

802   Figure 5 - Example of ITCZ detection in the east Pacific using the statistical model for 18

803   August 2000 at 2100 UTC. Shading represents IR temperature from GridSat, the black line

804   outlines the identified location of the ITCZ. The North American coastline is outlined in white.

GIF/SWF
805

806   Animation location:

807   ftp://ftp.ncdc.noaa.gov/pub/data/papers/bams_grisat/IRloop.gif or

808   ftp://eclipse.ncdc.noaa.gov/pub/misc/kknapp/bams_grisat/IRloop.gif or

809   ftp://eclipse.ncdc.noaa.gov/pub/misc/kknapp/bams_grisat/IRloop.swf

810

811
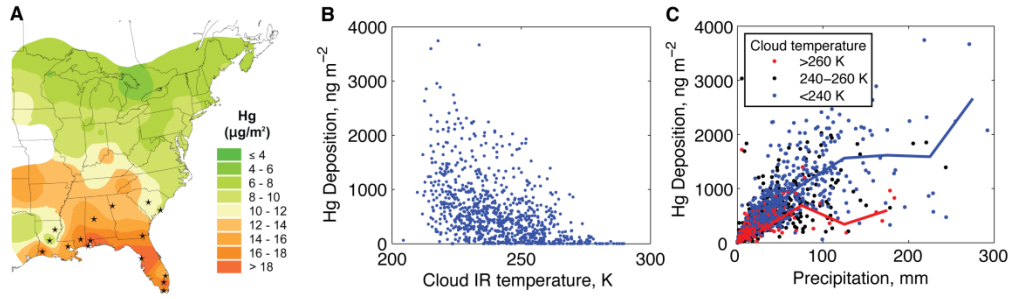
812

813   Figure 6 - (A) Mercury wet deposition in the eastern United States for 2005. Stars show sites

814   analyzed here. (B) Mercury wet deposition for summers 2001-2006 and mean infrared (IR) cloud

815   temperature from GridSat IR. See text for IR temperature averaging method. (C) Mercury wet

816   deposition and precipitation for three different cloud temperature ranges. Lines show mean

817   concentration in 50 mm precipitation bins for the coldest (temperature < 240K) and warmest

818   (temperature > 260K) clouds. [Figure adapted from (Holmes 2008, 2010) with deposition map

819   adapted from (Mercury Deposition Network 2006)]

820

821
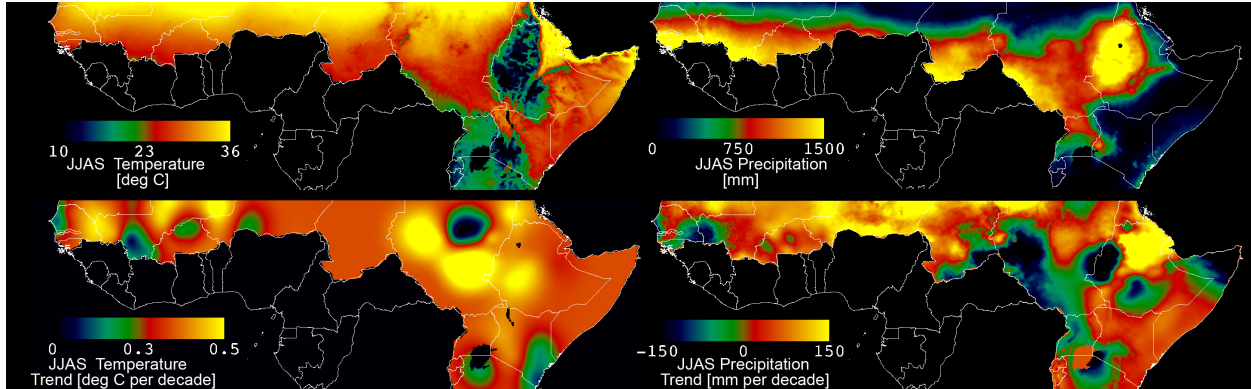
822

823

824   Figure 7 – July-September (JJAS) air temperature and rainfall estimates based on combinations

825   of GridSat infrared fields and in situ station observations. The top two panels show decadal

826   average air temperature (left) and rainfall (right) for the 1999-2008 period. The bottom panels

827   show the differences between these decadal averages and the 1984-1993 average (the 1999-2008

828   average minus the 1984-1993 average).

829

830

831

Figure 8 - Comparison of diurnal OLR models from the HIRS climatology and GridSat for August 2002. The GridSat OLR helps to verify the representativeness of the climatological OLR diurnal models used in the production of the HIRS OLR climate data record. The arrows in the central panel indicate the phases of the OLR diurnal models with the 12 o'clock local time pointing north, running counter-clockwise. The surrounding plots compare the diurnal models for selected regions with distinctively different types of diurnal variations. The mean values of GridSat OLR in each diurnal plot were adjusted to those of the HIRS to aid visual comparison.

842

```
#!/bin/bash

for hour in 00 03 06 09 12 15 18 21
do
  ncra GRIDSAT-B1.2002.07.??.$hour.nc \
      -d lat,10.,40. -d lon,-20.,45. -v irwin \
      -o GRIDSAT-B1.2002.07.$hour.nc
done
ncrcat GRIDSAT-B1.2002.07.??.nc -o GRIDSAT-B1.2002.07.nc
```

843

844   Figure SB1 – BASH code that uses netCDF operators to process one month of GridSat data of

845   the Sahara Desert into diurnally-averaged brightness temperatures.

846
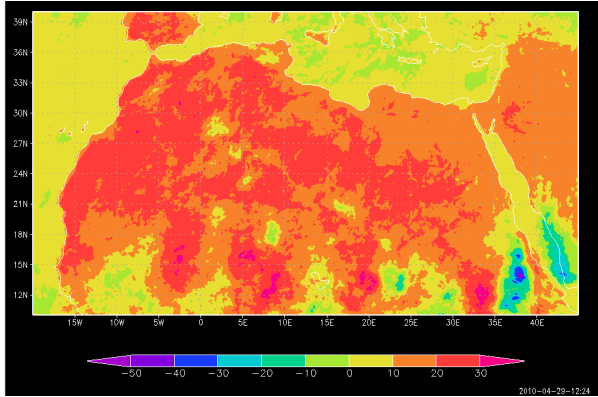
847

848   Figure SB2 – Average daily temperature change (K) between 3 UTC and 15 UTC over the

849   Saharan desert for August 2002.

Globally Gridded Satellite (GridSat) Observations for Climate Studies

Kenneth R. Knapp[1], Steve Ansari[1], Caroline Bain[2], Mark A. Bourassa[3], Michael J. Dickinson[4], Chris Funk[5], Chip N. Helms[6], Christopher C. Hennon[7], Christopher D. Holmes[8], George J. Huffman[9], James P. Kossin[1], Hai-Tien Lee[10], Alexander Loew[11], Gudrun Magnusdottir[12]

1   NOAA National Climatic Data Center
2   Univ. of California at Irvine (now at Met Office, Exeter, Devon, UK)
3   Florida State Univ.
4   Dept. of Earth and Atmospheric Sciences, The Univ. at Albany/SUNY (now at WeatherPredict Consulting, Wakefield, RI)
5   USGS Center for Earth Resource Observations and Science
6   Univ. of North Carolina Asheville (now at Florida State Univ.)
7   Univ. of North Carolina Asheville
8   Dept. of Earth and Planetary Science, Harvard Univ.
9   Science Systems and Applications, Inc. and NASA Goddard Space Flight Center
10 Cooperative Institute for Climate Studies, Univ. of Maryland, College ParK
11 Max-Planck-Institute for Meteorology, KlimaCampus, Hamburg, Germany
12 Univ. of California at Irvine

Geostationary satellites, each of which continually observes the same part of the Earth, have provided routine, fine-scale Earth observations since the 1970s. Despite the long period of record, use of these data in climate studies has proved to be difficult. Historically, each satellite operator has maintained an independent archive center. In part, this has been true because the full-resolution data are quite voluminous, even by modern standards. Another issue is that the data have been stored using diverse formats that vary between centers, and even within each center. Taken together, these issues have effectively prevented the uniform processing needed for long-term multi-satellite climate studies. The International Satellite Cloud Climatology Project set the stage for overcoming these issues by archiving a subset of the full resolution geostationary data at ~10 km resolution at 3 hourly intervals beginning in 1983. This intermediate archive overcame the first two issues, but not the third. Starting about five years ago, the NOAA National Climatic Data Center undertook the task of providing convenient access to these data by remapping the data to a standard map projection, recalibrating the data to optimize homogeneity over time, correcting for biases due to varying zenith view angles, and reformatting the data for broad public distribution. As a bonus, they incorporated additional geosynchronous data that extend the record back to 1980. The resulting Gridded Satellite (GridSat) dataset provides observations recorded by three different sensor channels. Two of these channels have been used on the geosynchronous satellites from the beginning of the record, and the third came into general use in the 1990s. A final design issue is that the satellites usually have some overlapping coverage in space at each time. While some users simply want a "best" global map, others want to see the complete data coverage for a particular satellite. We developed an innovative data layering approach that provides the single global map at each time, allows access to complete satellite data, and minimizes wasted storage space. The GridSat data

are already in use by the meteorological community. Examples include reanalysis of tropical cyclones, studies of global precipitation, and detection and tracking of the Intertropical Convergence Zone.